Journal of The
Electrochemical Society

Minimizing Experimental Effort: A Two-Equation Model for Wide-Range Ionic Conductivity in Lithium-Ion Battery Electrolytes

To cite this article: Maximilian Gruber *et al* 2026 *J. Electrochem. Soc.* **173** 120518

Journal of The Electrochemical Society, 2026 **173** 120518

Minimizing Experimental Effort: A Two-Equation Model for Wide-Range Ionic Conductivity in Lithium-Ion Battery Electrolytes

Maximilian Gruber,[1,2,z] Daniel Rutz,[1] Frank Hofmann,[1] and André Weber[2,3]

[1]*Mercedes-Benz AG, 70372 Stuttgart, Germany*
[2]*Karlsruhe Institute of Technology (KIT), Institute for Applied Materials (IAM-ET), 76131 Karlsruhe, Germany*

For concentrated lithium-ion battery electrolytes, ion association and ion crowding cause the ionic conductivity σ to deviate from the classical Walden rule, and existing empirical equations require dense grid-based measurement campaigns to capture these deviations. We derive a density-corrected Walden (DCW) equation that introduces the solution density ρ as a second transport descriptor alongside the dynamic viscosity η; the model contains two free parameters and is calibratable by linear regression. A complementary mass-action model, based on the classical ion-association equilibrium, separates ion pairing from ionic mobility and yields a physically interpretable dissociation profile. Both models are validated on $LiPF_6$ in EC:DMC:EMC spanning 0.25 mol L^{-1} to 3.00 mol L^{-1} and −20 to 45 °C. Using only three calibration concentrations, the DCW model reconstructs the full $\sigma(c, T)$ surface with a root-mean-square error of 0.27 mS cm^{-1}, approaching the accuracy of established benchmark Eqs. that require 5 to 10 calibration concentrations. Cross-validation on LiFSI in three pure solvents confirms transferability to other salt–solvent systems. The deterministic σ–η–ρ link additionally enables real-time quality control of conductivity measurements.
 [DOI: 10.1149/1945-7111/ae7d5b]

Manuscript received April 9, 2026. Published June 24, 2026.

Supplementary material for this article is available online

The electrolyte is a key component governing the rate capability, temperature performance, and cycle life of lithium-ion batteries.[1,2] The relevant transport properties include the ionic conductivity σ, the apparent salt diffusion coefficient D_{app}, and the apparent cationic transference number t_+^{app}. Of these, the ionic conductivity is the most readily accessible quantity. It therefore serves as a primary screening parameter for electrolyte formulations.[3,4] Its dependence on salt concentration c and temperature T determines the ohmic potential drop in the electrolyte phase. Consequently, $\sigma(c, T)$ indirectly influences the onset of lithium plating, the achievable fast-charging rate, and the overall power density of a cell.[5,6]

Electrochemical pseudo-two-dimensional (P2D) models, as originally formulated by Doyle, Fuller, and Newman,[7,8] require continuous, differentiable descriptions of all electrolyte transport properties as functions of both concentration and temperature. During medium- and high-rate operation, strong concentration gradients develop, ranging from near-depletion at one electrode to values exceeding 2 mol L^{-1} at the other.[5] The parametric functions must therefore faithfully represent $\sigma(c, T)$ over the entire accessible range. Inaccurate or incomplete parameterizations of electrolyte transport properties have been shown to produce erroneous predictions of cell voltage, lithium-plating onset, and thermal behavior.[5,6]

The prevailing approach to obtain such parameterizations involves systematic grid-based measurement campaigns, in which the ionic conductivity is determined at a dense matrix of discrete concentration and temperature points.[5,6,9] The comprehensive dataset reported by Landesfeind[9] covers 0.1 mol L^{-1} to 3.0 mol L^{-1} $LiPF_6$ at −10 °C to 50 °C in three solvent systems. The conductivity measurement alone required a dedicated Pt-microelectrode cell. Careful temperature equilibration at each set point added further effort. Including the additional determination of the apparent diffusion coefficient and transference number, a full transport characterization constitutes a substantial experimental effort[10] that limits the throughput of electrolyte screening and optimization.

The measured conductivity dataset is typically represented by empirical fitting functions. The equation proposed by Casteel and Amis[11] describes $\sigma(c)$ at a fixed temperature using four adjustable parameters and reproduces the characteristic bell-shaped conductivity curve with high accuracy. Extensions incorporating temperature dependence have been proposed,[12,13] and Landesfeind et al.[9] introduced a six-parameter rational function that simultaneously captures the concentration and temperature dependence of σ. While both approaches provide excellent interpolation within the measured data range, their purely empirical character limits their predictive capability outside the calibration domain. Extrapolation to concentrations or temperatures outside the training data can lead to unphysical behavior. This is a critical shortcoming for battery-cell parameterizations.

Alternative approaches include molecular-level models such as the Advanced Electrolyte Model,[14,15] which predict transport properties from speciation parameters, and machine-learning methods[16,17] that require large training datasets. Neither approach exploits the correlation between σ and the complementary transport properties viscosity and density to reduce the number of required conductivity measurements.

In this work, we propose an approach to parameterize the ionic conductivity of carbonate-based lithium-salt electrolytes that leverages complementary measurements of viscosity η and density ρ. The number of required conductivity measurements can thereby be reduced to as few as three calibration concentrations.

Two models are compared. The first is an empirical log-linear density-corrected Walden (DCW) equation with three adjustable parameters (A, α, γ). The second is a mass-action ion-pairing model[18,19] with three physically interpretable parameters. Both models are calibrated on $LiPF_6$ in EC:DMC:EMC (30:35:35 vol %) with 1.5 wt % VC. They are validated against literature data for LiFSI in DMC, EC, and PC reported by Neuhaus et al.[20] Their extrapolation performance is benchmarked against the Casteel–Amis[11] and Landesfeind[9] equations. Beyond parameterization, the deterministic link between σ, η, and ρ enables the models to serve as measurement consistency checks during electrolyte screening campaigns[21] (discussed below).

Both models rest on the approximate proportionality between σ and c/η, which holds for an ideal, fully dissociated electrolyte obeying the Walden rule ($\Lambda \cdot \eta = \text{const}$).[22] In this context, an ideal electrolyte is one in which the salt is completely dissociated into free ions ($\alpha_{diss} = 1$), the ions migrate independently of one another, and their mobility is governed solely by the viscous drag of the solvent.

[3]Electrochemical Society Member.
[z]E-mail: maximilian.m.gruber@mercedes-benz.com

This ideal behavior is strictly valid only in the dilute regime ($c \lesssim 0.01$ mol L^{-1} in aqueous solutions), where interionic distances are large enough that ion–ion interactions are negligible.[18,23] At battery-relevant salt loadings (0.5 mol L^{-1} to 3.0 mol L^{-1}), the electrolyte is far from this ideal limit. Real electrolytes deviate from the ideal Walden proportionality through two principal mechanisms. First, *ion association*: dissolved salt ions form electrically neutral contact ion pairs or higher-order aggregates, reducing the effective number of charge carriers below the nominal salt concentration.[18,19] Second, *ion crowding*: at elevated concentrations, the increasing number density of ions and their solvation shells introduces steric packing constraints that impede ionic mobility beyond what the dynamic viscosity η alone captures.[24] The magnitude of the overall deviation is quantified by the fractional Walden exponent $\alpha < 1$ ($\Lambda \propto \eta^{-\alpha}$), which is widely used to diagnose ion association in electrolyte solutions.[19,25–28] The following Theory Section derives the DCW equation and adapts the classical mass-action framework into the two parameterization models evaluated in this work.

Theory

Density-corrected Walden equation.—As introduced above, the generalized Walden rule relates the molar conductivity $\Lambda = \sigma/c$ to the dynamic (shear) viscosity η through a power-law scaling,[22] such that $\sigma \propto c \cdot \eta^{-\alpha}$. We formulate an empirical two-parameter Walden conductivity equation in logarithmic form by grouping both quantities into the ratio c/η under a single fractional exponent α:

$$\log_{10}(\sigma) = \beta + \alpha \cdot \log_{10}\left(\frac{c}{\eta}\right) \qquad [1]$$

where $\beta = \log_{10}(\sigma)|_{c/\eta=1}$ is the Walden intercept, a system-specific constant that encapsulates the intrinsic ionic mobility of the salt–solvent combination at unit concentration-to-viscosity ratio. By grouping c and η, the model enforces $\sigma \propto c^{\alpha}\eta^{-\alpha}$. For $\alpha < 1$ (sub-Walden regime, cf.. the Introduction), this formulation captures both the viscous drag and the reduced effective charge-carrier concentration.[19,29] However, Eq. 1 does not account for the ion-crowding effects introduced above: at elevated salt concentrations, steric packing constraints impede ionic mobility beyond what η alone predicts.[24] An additional scaling variable is therefore needed.

The solution density ρ is a natural candidate for this role. At fixed solvent composition, ρ increases monotonically with the number of dissolved ions per unit volume ($n_{\text{ion}} = N_A \cdot c$) and thus directly tracks the degree of ion crowding. Han[30] confirmed this link through molecular dynamics simulations: even small density variations induce pronounced changes in the self-diffusion coefficients and solvation dynamics of lithium ions in nonaqueous electrolytes. These density-driven effects are not fully reflected in the dynamic viscosity, which averages over bulk momentum transfer rather than local ion–ion interactions. Density therefore serves as a complementary descriptor of the structural environment in which ion transport takes place.

We therefore extend the two-parameter Walden equation (Eq. 1) by a multiplicative density correction. In the power-law framework underlying the Walden rule, this amounts to appending a factor ρ^{γ}, so that $\sigma \propto (c/\eta)^{\alpha} \cdot \rho^{\gamma}$. Taking the base-10 logarithm converts this product into a sum and yields the density-corrected Walden (DCW) equation:

$$\log_{10}(\sigma) = A + \alpha \cdot \log_{10}\left(\frac{c}{\eta}\right) + \gamma \cdot \log_{10}(\rho) \qquad [2]$$

The offset A is the intercept of the log-linear regression. It absorbs all unit-dependent and system-specific constants not captured by the exponents α and γ, and has no standalone physical interpretation. It differs from the Walden intercept β Eq. 1 because the density term redistributes variance between the offset and the exponents. The exponent α retains its role as the fractional Walden exponent quantifying the coupling between ionic mobility and the inverse dynamic viscosity η^{-1}, and γ is the density exponent accounting for ion-crowding effects.

On physical grounds, $\gamma = 2$ is a plausible value. Deviations from ideal Walden conductivity that are not absorbed by the constant exponent α are expected to scale with the square of the ion number density, consistent with pairwise (two-body) interactions between ions. These include both the concentration-dependent enhancement of contact ion-pair formation and steric crowding between overlapping solvation shells. Because ρ increases approximately linearly with c over the investigated range (Fig. 1c), ρ^2 provides a tractable proxy for pairwise ion–ion interactions. Fixing $\gamma = 2$ reduces the DCW equation to a two-parameter model (A, α) that can be calibrated by ordinary linear regression in $\log_{10}$-space. Whether this integer constraint holds for the present electrolyte system is tested in the Results; its transferability to other solvent systems is examined in the literature validation below.

Mass-action ion-pairing model.—The DCW equation captures both ion association and ion crowding through two empirical exponents (α, γ), but does not separate the two mechanisms. A complementary approach, based on the classical mass-action treatment of ion association in electrolyte solutions,[18,19] models ion association explicitly through a chemical equilibrium. This yields a physically interpretable dissociation profile $\alpha_{\text{diss}}(c)$ and an association constant K_a that quantifies the propensity for ion-pair formation.

In a lithium-salt electrolyte, the nominal salt concentration c represents the sum of free (dissociated) ions and neutral ion pairs.

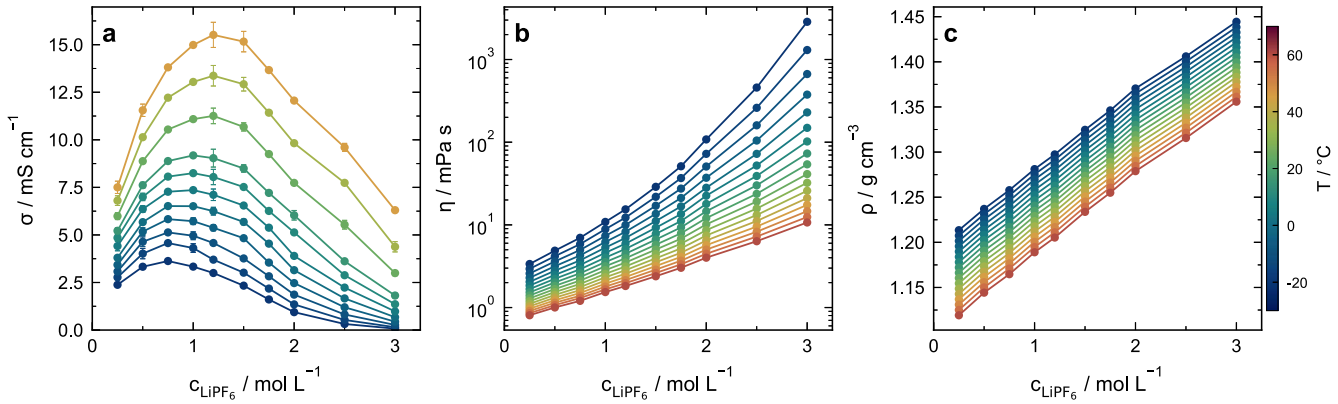

Figure 1. Concentration-dependent transport properties of $LiPF_6$ in EC:DMC:EMC (30:35:35 vol %, 1.5 wt % VC). (a) Ionic conductivity σ (−20 to 45 °C), (b) dynamic viscosity η (logarithmic ordinate), and (c) density ρ. Color coding by temperature; viscosity and density data extend to 60 °C. Error bars: standard deviation of three consecutive measurements.

For $LiPF_6$ dissolved in a carbonate solvent mixture, the relevant association equilibrium is:

$$Li^+(solv) + PF6^-(solv) \rightleftharpoons LiPF_6(solv) \quad [3]$$

where (solv) denotes solvation by the organic carbonate mixture. The equilibrium describes the reversible formation of electrically neutral contact ion pairs from solvated free ions; all three species remain in solution. Only the dissociated ions, present at the effective concentration $c \cdot \alpha_{diss}$, contribute to ionic charge transport, while the associated fraction $(1 - \alpha_{diss})$ is electrically neutral and does not contribute to the electrolyte's ionic conductivity. The macroscopic dynamic viscosity η governs the frictional drag on the mobile ions, so that their mobility scales with the inverse dynamic viscosity of the medium.

The degree of dissociation α_{diss} is determined by the mass-action equilibrium. Defining the association constant K_a as the ratio of ion-pair to free-ion concentrations:

$$K_a = \frac{1 - \alpha_{diss}}{\alpha_{diss}^2 \cdot c} \quad [4]$$

and solving the resulting quadratic equation for α_{diss} yields:

$$\alpha_{diss} = \frac{-1 + \sqrt{1 + 4\,K_a\,c}}{2\,K_a\,c} \quad [5]$$

In the dilute limit ($K_a \cdot c \ll 1$), $\alpha_{diss} \to 1$, and the salt is fully dissociated. At higher concentrations, α_{diss} decreases progressively, reflecting increasing ion association. The association constant K_a thus provides a single, physically interpretable parameter that quantifies the propensity for ion-pair formation in a given salt–-solvent combination.[19] As a thermodynamic equilibrium constant, K_a is in principle temperature-dependent ($K_a \propto \exp(-\Delta G°/RT)$); whether this dependence is significant for the present system is examined in the model comparison below.

The mass-action conductivity equation is derived in three steps. First, the generalized Walden rule states that the molar conductivity scales as a power law of the inverse dynamic viscosity:

$$\Lambda = \Lambda_\infty \cdot \eta^{-\alpha_W} \quad [6]$$

where Λ_∞ is an effective prefactor and α_W is the fractional Walden exponent. Second, only the fraction α_{diss} of the nominal salt concentration contributes to charge transport, so the effective charge-carrier concentration is $c_{free} = c \cdot \alpha_{diss}$. Third, combining both relations via $\sigma = \Lambda \cdot c_{free}$ yields the mass-action conductivity equation:

$$\sigma = \Lambda_\infty \cdot c \cdot \alpha_{diss}(c,\ K_a) \cdot \eta^{-\alpha_W} \quad [7]$$

The model contains three adjustable parameters: K_a (from the dissociation equilibrium, Eq. 4), Λ_∞, and α_W. The prefactor Λ_∞ has units that depend on α_W. The formulation employs the analytical concentration c rather than the thermodynamic activity $a = \gamma_\pm \cdot c$, where $\gamma_\pm$ is the mean ionic activity coefficient. This approximation is strictly valid at low to moderate concentrations where $\gamma_\pm \approx 1$. At high salt loadings ($c > 2$ mol L^{-1}), deviations may arise from the neglect of activity coefficients and the implicit assumption of a concentration-independent relative permittivity ε_r of the solvent mixture.[18] Despite these idealizations, Eq. 7 provides a framework in which the conductivity is directly coupled to the free-ion concentration $\alpha_{diss} \cdot c$ rather than the total salt concentration. This enables a physically meaningful separation of ion-pairing and mobility effects.

Experimental

Electrolyte solutions.—Commercial electrolyte solutions of $LiPF_6$ in EC:DMC:EMC (30:35:35 vol %) with 1.5 wt % vinylene carbonate (VC) were purchased from E-Lyte Innovations GmbH at ten salt concentrations: 0.25, 0.50, 0.75, 1.00, 1.20, 1.50, 1.75, 2.00, 2.50, and 3.00 mol L^{-1}. All solutions were stored and handled under argon atmosphere ($H_2O < 0.1$ ppm, $O_2 < 0.1$ ppm). Samples were transferred from the glove box to the measuring cell using gastight syringes to minimize atmospheric exposure.

Ionic conductivity.—The ionic conductivity σ was determined by potentiostatic electrochemical impedance spectroscopy (EIS) using a TSC 1600 Closed measuring cell (rhd instruments GmbH & Co. KG).[31] Both a platinum/platinum (Pt/Pt) and a glassy-carbon/platinum (GC/Pt) electrode configuration were employed to verify that the electrode material does not influence the measured conductivity. Both configurations yielded reproducible values within the experimental uncertainty.

Cell preparation.—Prior to each measurement series, the conductivity cell was cleaned with deionized water, rinsed with isopropanol, and dried in a vacuum oven for at least 10 h. The dried cell was transferred directly into the argon-filled glove box without long ambient exposure and filled with the respective electrolyte solution. This cleaning protocol was found to be essential for obtaining reproducible EIS spectra.

Calibration.—The cell constant K_{cell} is a geometric factor (unit: cm^{-1}) that relates the measured electrical resistance to the specific conductivity of the solution via $\sigma = K_{cell}/R_s$.[32] It depends on the electrode area and the inter-electrode distance of the particular cell and must therefore be determined experimentally for each cell geometry. K_{cell} was calibrated using a traceable KCl conductivity standard (12 880 µS cm^{-1} at 25 °C; Hanna Instruments HI-70030P), following the procedure described by Drüschler et al.[31]

EIS measurement and evaluation.—EIS spectra were recorded using a BioLogic VMP-300 potentiostat with an excitation amplitude of 10 mV (rms) over a frequency range from 1 kHz to 7 MHz. At each temperature, three consecutive spectra were acquired to verify the absence of electrode contamination or spectral drift. The electrolyte bulk resistance R_s was extracted by fitting the EIS data to an equivalent circuit consisting of a series inductance L, a series resistor R_s, and a constant-phase element (CPE). The inductance element accounts for parasitic inductive contributions from the cell and wiring that become significant at high frequencies.[32] The CPE replaces an ideal capacitor to account for the non-ideal capacitive response of the electrode–electrolyte interface.[32] The bulk resistance R_s corresponds to the high-frequency real-axis intercept of the impedance arc and was extracted from the equivalent-circuit fit. The ionic conductivity was calculated from $\sigma = K_{cell}/R_s$.

Temperature protocol.—Measurements were performed at eleven temperatures: −20, −15, −10, −5, 0, 5, 10, 15, 25, 35, and 45 °C. To minimize the risk of electrolyte evaporation affecting the low-temperature data, the following sequence was adopted: (i) an initial reference measurement at 25 °C; (ii) stepwise cooling to −20 °C; (iii) stepwise heating to 45 °C; and (iv) a final control measurement at 25 °C. Agreement between the initial and final 25 °C values confirmed that neither significant electrolyte degradation nor electrode fouling occurred during the temperature sweep. After each temperature change, a thermal equilibration time of 3 h was allowed before recording the EIS spectrum. Each reported conductivity value represents the mean of three consecutive measurements; the error bars indicate the experimental standard deviation.

Viscosity and density.—The dynamic viscosity η and density ρ were measured simultaneously using a Stabinger-type viscometer with an integrated oscillating U-tube density cell (SVM 3001, Anton Paar GmbH) in accordance with ASTM D7042.[33] A single measurement cycle yields both quantities from a sample volume of approximately 2.5 mL. Measurements were performed at seventeen temperatures from −20 °C to 60 °C in 5 °C steps.

Data analysis and model calibration.—Both models (Eqs. 2 and 7) were fitted to the full conductivity dataset (Sections –). The DCW equation was fitted by minimization of the log-transformed residuals in $\log_{10}(\sigma)$ space using ordinary linear regression. The mass-action model was fitted by minimization of the linear-scale residuals via nonlinear least-squares optimization (`scipy.optimize.curve_fit`) with box-constrained parameter bounds. Because the objective function is evaluated in $\log_{10}(\sigma)$ space, goodness-of-fit metrics are reported in both domains. For each model, we quote $R^2_{\log}$ and R^2_{lin} as well as the root-mean-square error (RMSE) in the respective fitting domain and on the linear scale.

To evaluate the extrapolation capability of each model, a reduced calibration protocol is employed. Only three concentrations (0.25, 1.20, and 3.00 mol L^{-1}) are used for parameter estimation, while the remaining seven concentrations serve as blind validation points. The viscosity $\eta(c)$ and density $\rho(c)$ at intermediate concentrations are interpolated from the same three calibration points using second-order polynomials in c, applied to $\log_{10}\eta$ and ρ, respectively. The predicted $\sigma(c)$ curves are then compared with the full experimental dataset at each temperature. This protocol mimics a practical scenario in which a minimal number of labor-intensive conductivity measurements is supplemented by comparatively rapid viscosity and density determinations.

The extrapolation performance of the DCW and mass-action models is benchmarked against the Casteel–Amis[11] and Landesfeind[9] equations introduced in the Introduction. Both reference models are fitted to the full dataset (all ten concentrations and eleven temperatures) and thus serve as upper-bound benchmarks for what is achievable with comprehensive grid-based data.

To determine the minimum required number of calibration concentrations, a combinatorial resampling analysis was performed: for each n from 3 to 10, all possible combinations (or a random subset of up to 200) of n concentrations were drawn from the ten available values, the models calibrated, and the prediction RMSE evaluated against the full dataset.

Model transferability is assessed by applying both models to independent literature data reported by Neuhaus et al.[20,34] for lithium bis(fluorosulfonyl)imide (LiFSI) dissolved in the pure solvents DMC, EC, and propylene carbonate (PC). This tests whether the functional form generalizes to a different lithium salt and to single-solvent systems. Because the $\gamma = 2$ constraint was established for the primary system, the density exponent is left as a free parameter in the literature fits, separating the general model structure from the system-specific constraint.

Results and Discussion

Raw data overview.—Figure 1 presents the measured ionic conductivity σ, dynamic viscosity η, and density ρ as a function of salt concentration for all investigated temperatures. The conductivity dataset spans 110 conditions (10 concentrations, 11 isotherms); viscosity and density cover an extended grid of 170 conditions up to 60 °C. The ionic conductivity exhibits the characteristic non-linear

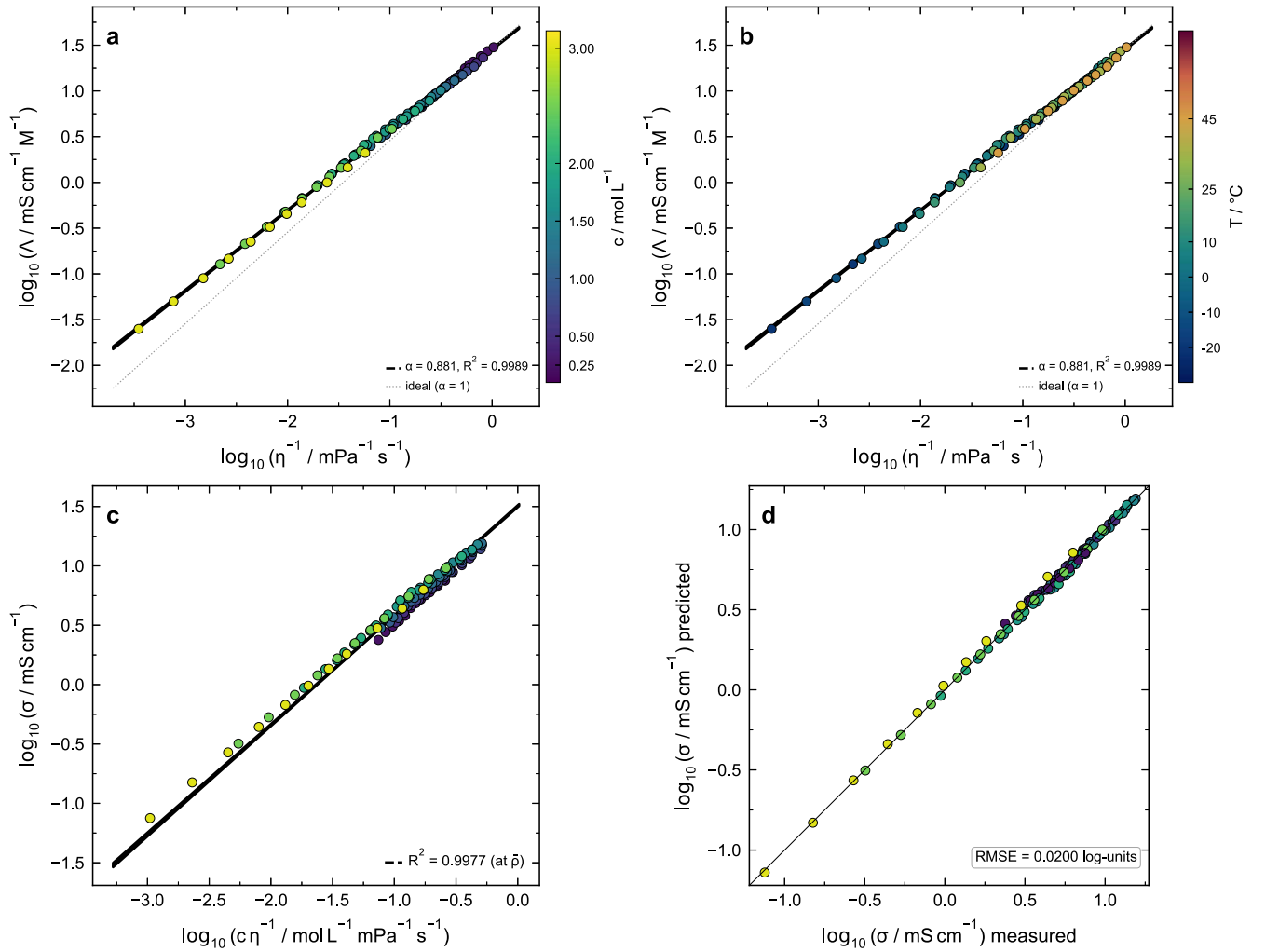

Figure 2. Walden analysis. (a) $\log_{10}(\Lambda)$ vs. $\log_{10}(\eta^{-1})$, color-coded by concentration; (b) same data, color-coded by temperature; dotted line: ideal Walden limit ($\alpha = 1$). (c) $\log_{10}(\sigma)$ vs. $\log_{10}(c/\eta)$; dashed line: DCW model (Eq. 2) at mean density $\bar{\rho}$. (d) Parity plot of predicted vs. measured $\log_{10}(\sigma)$ ($R^2 = 0.9977$, RMSE =0.020 log-units). Shaded bands: 95 % confidence intervals.

concentration dependence typical of concentrated electrolytes.[5] σ increases steeply at low concentrations, passes through a maximum near 0.75 mol L^{-1} to 1.20 mol L^{-1} depending on temperature, and decreases at higher salt loadings. This bell-shaped behavior reflects the interplay between increasing charge-carrier density and rising viscous drag with concentration.[5] The viscosity increases monotonically and approximately exponentially with c at all temperatures (Fig. 1b, note the logarithmic ordinate), while the density shows a near-linear increase (Fig. 1c). All three properties exhibit a strong temperature dependence, spanning nearly an order of magnitude in σ and η between −20 °C and 45 °C. This underscores the necessity of a parameterization that captures the full concentration and temperature domain simultaneously.

Walden analysis and density-corrected Walden equation.— Figure 2 shows the Walden analysis of the conductivity data. In the classical Walden representation (Fig. 2a, 2b), the molar conductivity $\Lambda = \sigma/c$ is plotted against the inverse viscosity η^{-1} on logarithmic axes. The experimental data for all concentrations and temperatures fall below the ideal Walden line ($\alpha = 1$), following a power-law scaling with a fractional exponent $\alpha = 0.881 \pm 0.003$ (dashed line, $R^2 = 0.9989$, RMSE =0.020 log-units in the $\log_{10}\Lambda$ domain). This sub-Walden scaling is consistent with the ion-association mechanism introduced above.[19,22,27] When color-coded by concentration (Fig. 2a), a systematic vertical spread becomes evident: at a given value of η^{-1}, higher-concentration solutions exhibit lower molar conductivity than predicted by Eq. 1. This concentration-dependent residual structure reflects the ion-crowding contribution introduced above that the classical Walden equation cannot capture.

The color-coding by temperature (Fig. 2b) reveals that the Walden exponent is approximately temperature-invariant: all isotherms collapse onto a single band that is well described by the fitted Walden line.[35] This observation supports the interpretation that the fractional exponent α reflects a structural property of the ion–solvent system, namely the propensity for ion association, rather than a thermally activated process.[35]

Figure 2c replots the same data as $\log_{10}(\sigma)$ versus $\log_{10}(c/\eta)$. Unlike the classical Walden plot, c is now part of the x-axis variable rather than separated out via $\Lambda = \sigma/c$. This change of variables absorbs the dominant concentration dependence and visibly tightens the data cloud compared with Fig. 2a. A fit of the Walden equation (Eq. 1) without density correction yields $R^2 = 0.9915$ and an RMSE of 0.039 log-units in $\log_{10}(\sigma)$. The remaining vertical scatter is not

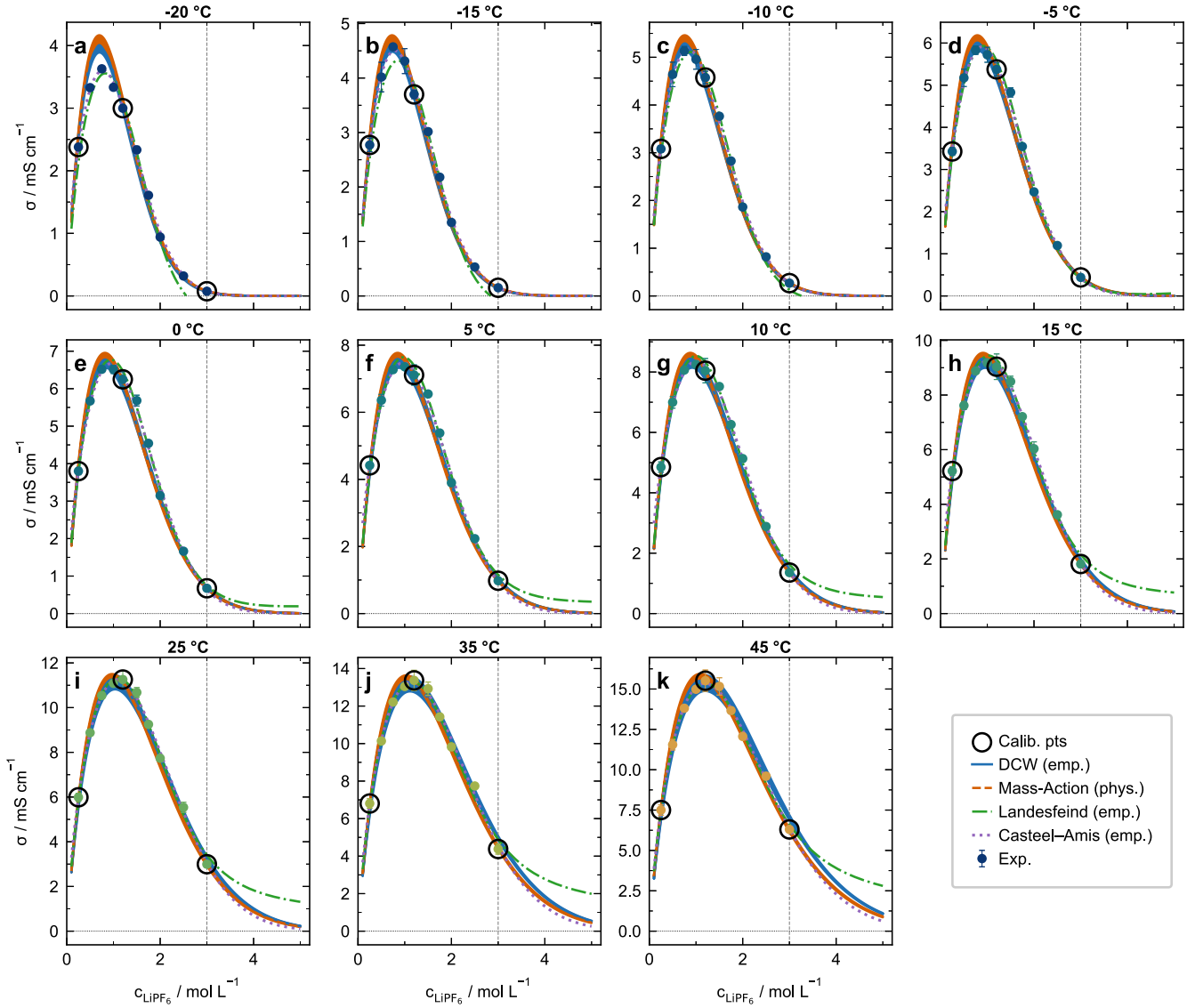

Figure 3. Three-point extrapolation of $\sigma(c)$ at each temperature. Open circles: calibration concentrations (0.25, 1.20, and 3.00 mol L^{-1}); filled circles: measured data. Solid blue: DCW ($\gamma = 2$); dashed orange: mass-action model. Dash-dotted green: Landesfeind et al.[9]; dotted purple: Casteel–Amis[11], both fitted to all ten concentrations. Shaded bands: 95 % confidence intervals.

Table I. Fit parameters and statistical metrics for the DCW equation ($\gamma = 2$ fixed) and mass-action model fitted to the full $LiPF_6$/EC:DMC:EMC dataset (110 data points, 0.25 mol L^{-1} to 3.00 mol L^{-1}, −20 °C to 45 °C for conductivity). Uncertainties are standard errors from the covariance matrix.

Parameter	DCW equation	Mass-action model
A (offset)	1.285 ± 0.004	—
α / α_W (Walden exponent)	0.922 ± 0.004	0.834 ± 0.007
γ (density exponent)	2 (fixed)	—
K_a / L mol^{-1}	—	0.040 ± 0.012
Λ_∞ / mS cm^{-1} M^{-1} (mPa s)$^{\alpha_W}$	—	27.64 ± 0.23
R^2 ($\log_{10}\sigma$)	0.9977	0.9945
RMSE ($\log_{10}\sigma$) / log-units	0.020	0.031
R^2 (σ, linear scale)	0.9961	0.9962
RMSE / mS cm^{-1}	0.236	0.233

random: at a given c/η, denser (i.e. more concentrated) solutions lie systematically below less concentrated ones. This pattern is the fingerprint of ion crowding (see the Theory): the ion number density grows with c, intensifying pairwise interactions that reduce conductivity beyond what η alone accounts for.

The density exponent γ in the DCW equation (Eq. 2) captures this density-dependent variance. Fitting γ as a free parameter yields $\gamma = 1.97 \pm 0.11$, statistically indistinguishable from the integer 2 predicted by the pairwise-interaction argument in the Theory above. Fixing $\gamma = 2$ does not degrade the fit quality and reduces the model to two free parameters: $A = 1.2853 \pm 0.0041$ and $\alpha = 0.9215 \pm 0.0039$. The DCW exponent α is numerically larger than the classical Walden exponent (0.881, Fig. 2a). The ρ^2 term absorbs part of the concentration-dependent deviation that the classical fit projects entirely onto α. The dashed line in Fig. 2c shows the DCW model at the dataset-averaged density $\bar{\rho}$. Because Eq. 2 depends on three input variables (c, η, ρ), this projection to $\rho = \bar{\rho}$ is necessary to display the model in two dimensions. The parity plot (Fig. 2d), in which each data point is evaluated at its actual density, achieves $R^2 = 0.9977$ and an RMSE of 0.020 log-units. The density correction thus halves the RMSE compared with Eq. 1 alone (0.039 → 0.020 log-units) and improves R^2 from 0.9915 to 0.9977.

Conductivity extrapolation from three calibration points.—Figure 3 tests whether the DCW and mass-action models can reconstruct the full $\sigma(c)$ curve from only three calibration concentrations (0.25, 1.20, and 3.00 mol L^{-1}; open circles). The results are compared against the Landesfeind (six-parameter)[9] and Casteel–Amis (four-parameter)[11] benchmarks described in the Experimental section.

Despite using only three calibration points, both Walden-based models reproduce the measured $\sigma(c)$ curves at all temperatures, including the position and height of the conductivity maximum. The three-point DCW fit ($\gamma = 2$ fixed) yields $A = 1.280 \pm 0.008$ and $\alpha = 0.926 \pm 0.007$; the mass-action fit yields $K_a = 0.094 \pm 0.014$ L mol-1, $\Lambda_\infty = 30.0 \pm 0.2$, and $\alpha_W = 0.861 \pm 0.006$. These values agree closely with the full-dataset estimates in Table I. The prediction RMSE of the three-point DCW model is 0.27 mS cm^{-1}, approaching the accuracy of the benchmark models that require all ten concentrations.

Even with all three DCW parameters free, the three-point fit achieves an RMSE of 0.34 mS cm^{-1}, already comparable to the benchmark models trained on ten concentrations. However, the fitted $\gamma = 1.33 \pm 0.14$ is biased low relative to the full-dataset estimate of 1.97 ± 0.11, because three concentrations provide limited density variation. Fixing $\gamma = 2$ removes this bias and further reduces the RMSE to 0.27 mS cm^{-1}, a 20 % improvement with one fewer free parameter.

The Walden-based models also extrapolate more reliably than the empirical benchmarks. When trained on $c \leqslant 2.0$ mol L^{-1} and evaluated at 2.5 and 3.0 mol L^{-1}, the DCW model achieves an RMSE of 0.19 mS cm^{-1}, two to three times lower than the Landesfeind (0.44 mS cm^{-1}) and Casteel–Amis (0.59 mS cm^{-1}) equations. The empirical functions lack physical constraints on the high-concentration tail and can diverge outside the training domain. The Walden-based models remain bounded by the auxiliary $\eta(c)$ and $\rho(c)$ data, which anchor the prediction even at untrained concentrations.

No additional experiments beyond the three calibration samples are required (Fig. 3). Conductivity measurements by EIS remain necessary at the three calibration concentrations; the η and ρ values at intermediate concentrations are interpolated from the calibration data (see the Experimental section). Because each viscometry measurement co-determines η and ρ (see above), the per-sample effort is minimal compared with EIS-based conductivity determinations.[36]

Quantitative model comparison.—Figure 4 compares the DCW and mass-action models fitted to the full dataset (110 data points). The parity plots (Figs. 4a, 4b) show predicted versus measured conductivity on linear axes, color-coded by concentration. Both models achieve $R^2_{lin} > 0.996$ and linear-scale RMSE values of 0.236 mS cm^{-1} (DCW) and 0.233 mS cm^{-1} (mass-action), respectively (Table I). The DCW equation yields a slightly better fit in the logarithmic domain; the mass-action model matches it on the linear scale. With 110 data points and only two (DCW) or three (mass-action) free parameters, overfitting is excluded.

The relative residuals (Fig. 4c) show the error structure across concentration and temperature. For the DCW model (diamonds), the residuals scatter symmetrically around zero with no systematic trend. The median absolute residual is approximately 2 % for both models over the range 0.75 mol L^{-1} to 2.50 mol L^{-1}. Individual deviations can reach 8 % (DCW) and 10 % (mass-action) at the boundaries of this range. The largest mass-action errors occur at $c = 3.00$ mol L^{-1} and $T \leqslant -10$ °C, where relative deviations exceed 20 %. At these conditions, the high electrolyte resistance shifts the impedance response out of the inductive regime: the spectra become purely capacitive within the accessible frequency window, so that the parasitic inductance L in the equivalent circuit (see the EIS evaluation above) can no longer be resolved. Because the fit cannot separate L from R_s, the extracted bulk resistance—and hence the reference σ—carries increased uncertainty at these extreme points. The DCW model is less affected (maximum 16 % at $T = -20$ °C), likely because the ρ^2 term provides an additional constraint at high concentrations.

Figure 4d shows the degree of dissociation $\alpha_{diss}(c)$ from the mass-action fit. The fitted association constant $K_a = 0.040$ L mol^{-1} indicates weak ion pairing. At 0.25 mol L^{-1}, $\alpha_{diss} \approx 0.99$ (nearly complete dissociation); at 3.00 mol L^{-1}, it decreases to approximately 0.90. This is consistent with the sub-Walden exponents from both the mass-action fit ($\alpha_W = 0.834$) and the classical Walden analysis ($\alpha = 0.881$, see above).[19,29] Thermodynamically, K_a should depend on temperature ($K_a \propto \exp(-\Delta G°/RT)$). Temperature-resolved fits, however, yield no systematic variation with T, so a single global K_a is used. The dissociation profile provides the effective free-ion concentration $c \cdot \alpha_{diss}$, which can serve as an independent consistency check on the charge-carrier assumptions embedded in P2D transport parameterizations.[3]

The two models serve complementary purposes. The DCW equation with $\gamma = 2$ reduces to a linear regression in log-space ($R^2_{log} = 0.9977$). It is suitable for applications requiring only an accurate $\sigma(c, T)$ surface, such as electrolyte screening or quality control. The mass-action model requires nonlinear optimization but provides K_a and $\alpha_{diss}(c)$, offering physical insight into the degree of ion pairing that complements the empirical DCW fit.

Literature validation on independent solvent systems.—Both models were applied to the independent LiFSI dataset of Neuhaus et al.[20] (see the Experimental section). Table II and Fig. 5 summarize the results for three pure solvents spanning a wide range of static

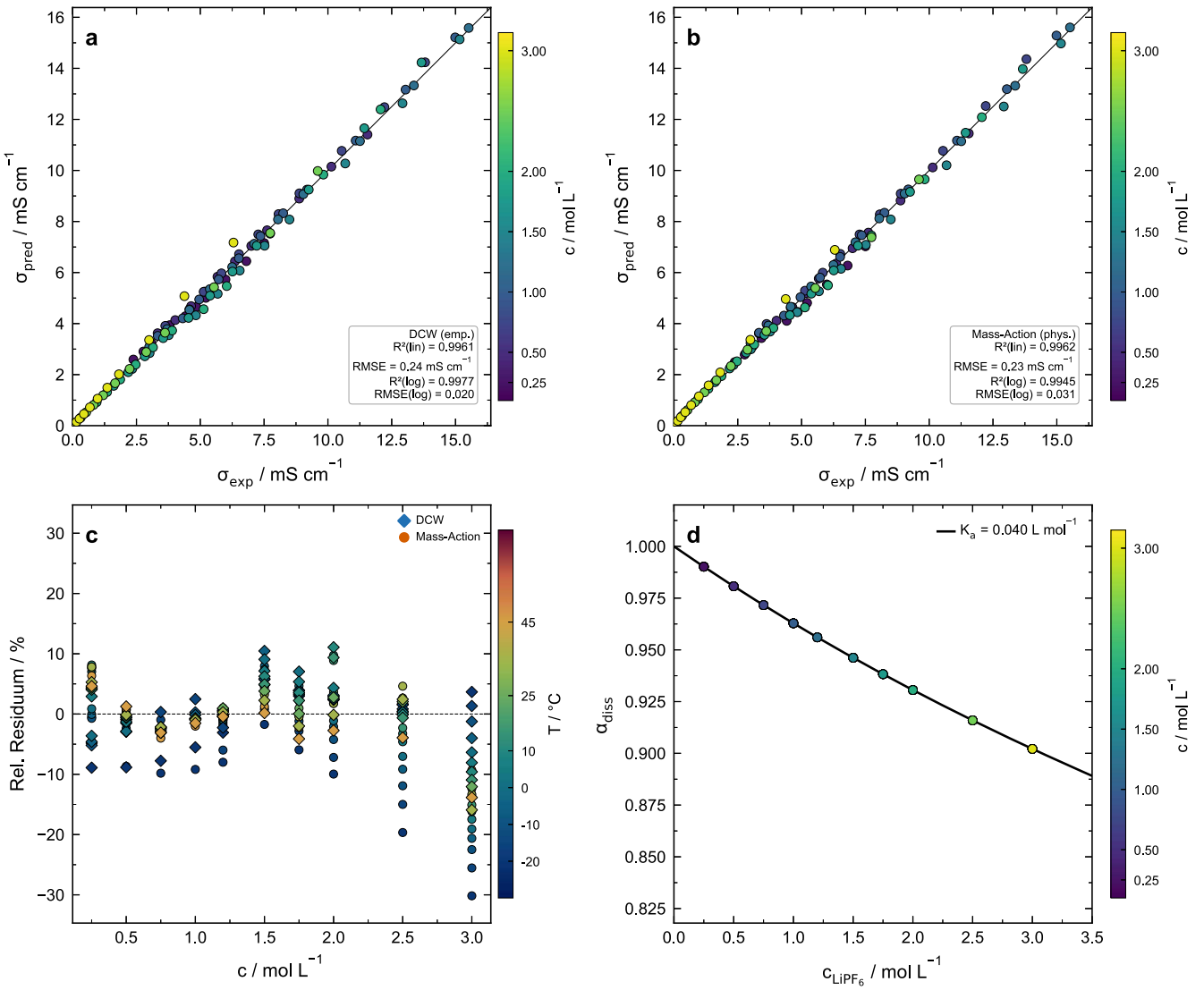

Figure 4. Full-dataset comparison of DCW and mass-action models (110 data points). (a),(b) Parity plots for DCW and mass-action, respectively, color-coded by concentration. (c) Relative residuals vs. concentration (diamonds: DCW; circles: mass-action), color-coded by temperature. (d) Degree of dissociation $\alpha_{\mathrm{diss}}(c)$ from the mass-action fit ($K_a = 0.040$ L mol^{-1}).

relative permittivities: $\varepsilon_r = 3.2$ (DMC), 61.4 (PC), and 89.7 (EC).[20] EC is solid below its melting point of ≈36 °C; its ε_r therefore refers to the liquid phase above this temperature. The available temperature range reflects this constraint: 40 °C to 60 °C for EC ($N = 18$), versus 0 °C to 60 °C for PC ($N = 32$) and 10 °C to 60 °C for DMC ($N = 32$).

For LiFSI in PC ($\varepsilon_r = 61.4$), both models achieve $R^2_{\mathrm{lin}} \geqslant 0.998$ with all residuals below ± 0.05 log-units. The Walden exponent $\alpha = 0.958 \pm 0.015$ is close to unity, consistent with nearly complete dissociation in this high-permittivity solvent.[19,27]

LiFSI in DMC ($\varepsilon_r = 3.2$) represents the opposite extreme. The Walden exponent drops to $\alpha = 0.350 \pm 0.058$, indicating extensive ion association.[19,26] The DCW model captures the overall trend ($R^2_{\mathrm{lin}} = 0.931$), but the mass-action model performs poorly ($R^2_{\mathrm{lin}} = 0.787$). A single 1: 1 association equilibrium cannot represent the triple ions and higher-order aggregates prevalent at $\varepsilon_r < 5$.[19,26]

LiFSI in EC ($\varepsilon_r = 89.7$) is a revealing edge case. Despite the highest permittivity of the three solvents, the Walden exponent is only $\alpha = 0.825 \pm 0.037$. Two effects contribute. The strong Lewis basicity of EC creates rigid solvation shells around Li^+, increasing the effective hydrodynamic radius.[1,37] Additionally, EC at 40 °C to 60 °C operates close to its melting point as a deeply structured liquid, where ionic mobility decouples from the macroscopic dynamic viscosity.[26,38] Both models accordingly show reduced fit quality (DCW: $R^2_{\mathrm{lin}} = 0.876$; MA: $R^2_{\mathrm{lin}} = 0.860$).

Table II. Literature validation: LiFSI in three pure solvents (data from Neuhaus et al.[20,34]). ε_r = static relative permittivity of the neat solvent; N = number of data points.

Solvent	ε_r	N	α (Walden)	R^2_{lin} DCW/MA	R^2_{log} DCW/MA
PC	61.4	32	0.958 ± 0.015	0.998/0.999	0.997/0.997
EC	89.7	18	0.825 ± 0.037	0.876/0.860	0.866/0.854
DMC	3.2	32	0.350 ± 0.058	0.931/0.787	0.971/0.846

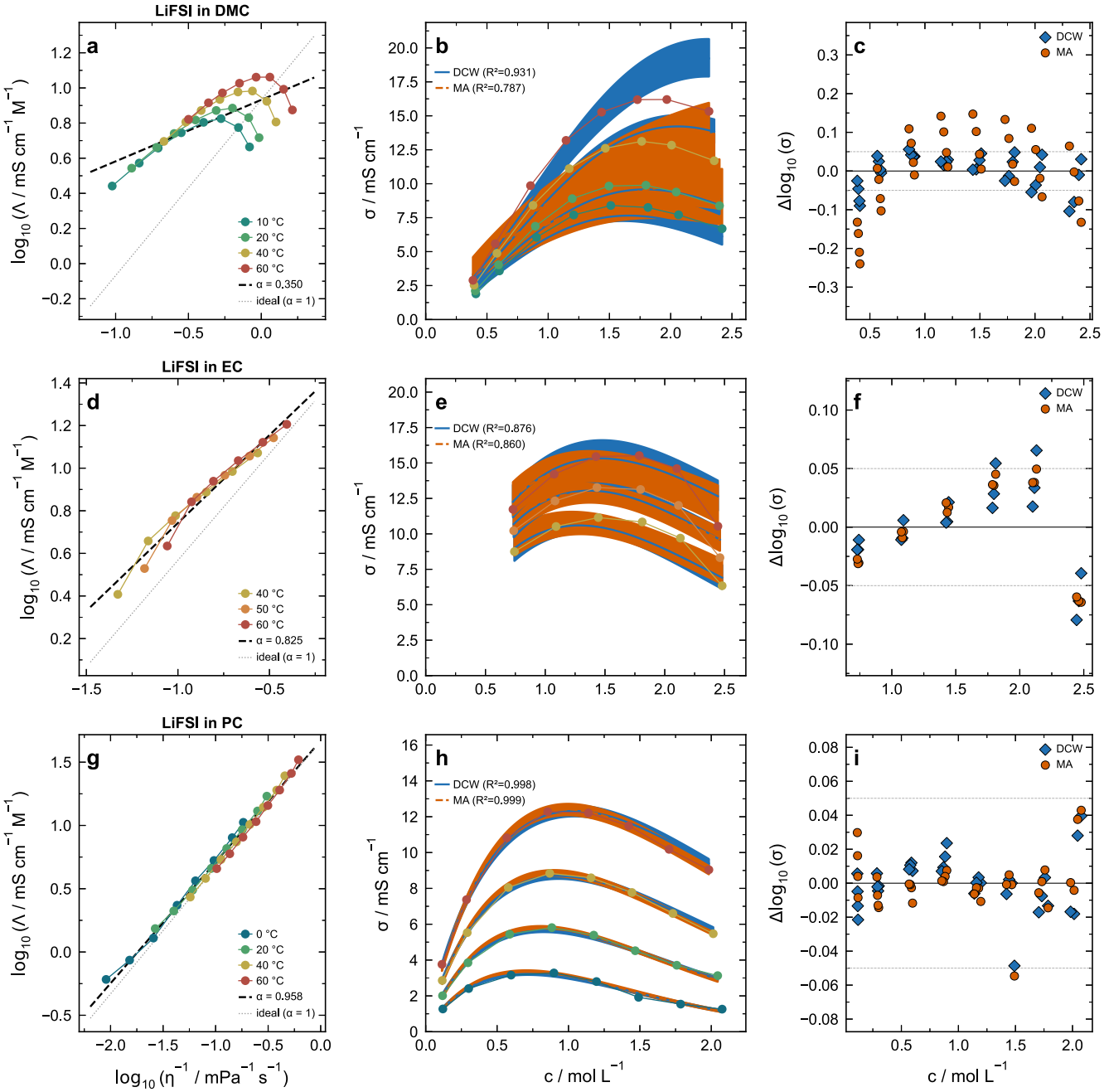

Figure 5. Cross-validation on independent LiFSI data (Neuhaus et al.[20,34]) in DMC (top), EC (middle), and PC (bottom). Left: Walden plots with fitted exponent α; center: $\sigma(c)$ with DCW (blue) and mass-action (orange) predictions; right: residuals $\Delta\log_{10}(\sigma)$. Shaded bands: 95 % confidence intervals.

The cross-validation delineates the scope of the Walden-based approach. Both models perform best for $\varepsilon_r > 20$, where neither extreme ion pairing nor anomalous solvation dominates.[1,39] Practical multi-component battery electrolytes typically fall in this range ($\varepsilon_r \approx 20$–40), and the two-parameter DCW equation provides $R^2 > 0.996$ under these conditions.

Optimal number of calibration points.—Figure 6 quantifies how the prediction error depends on the number of calibration concentrations n. For each n from 3 to 10, all possible n-point combinations (or up to 200 random draws) were tested via the combinatorial resampling protocol described in the Experimental section. Three model variants are compared: DCW with $\gamma = 2$ fixed, DCW with γ free, and the mass-action model.

For DCW ($\gamma = 2$), the median RMSE drops from 0.29 mS cm^{-1} ($n = 3$) to 0.25 mS cm^{-1} ($n = 5$) and plateaus at 0.24 mS cm^{-1} ($n = 7$). The mass-action model follows the same trend: 0.33 mS cm^{-1} ($n = 3$) to 0.24 mS cm^{-1} ($n = 10$). The marginal improvement per additional point is ≈0.04 mS cm-1 from $n = 3$ to $n = 4$. This gain already falls below the experimental reproducibility of 0.06 mS cm^{-1}. Beyond $n = 5$, additional measurements do not improve accuracy beyond experimental noise.

The comparison between DCW ($\gamma = 2$) and DCW (γ free) reveals the practical benefit of fixing the density exponent. At $n = 3$, the constrained model outperforms the free-γ variant by 7 % in median RMSE (0.29 vs. 0.31 mS cm^{-1}). This advantage diminishes with increasing n: at $n = 5$, the difference is only 3 %, and at $n \geqslant 7$, both variants effectively converge (≈1 %). The sparse density variation available at $n = 3$ biases the free γ estimate (see the extrapolation analysis above), whereas fixing $\gamma = 2$ stabilizes the fit. At $n \geqslant 5$, sufficient density variation is available to constrain γ reliably, making the choice between fixed and free γ inconsequential.

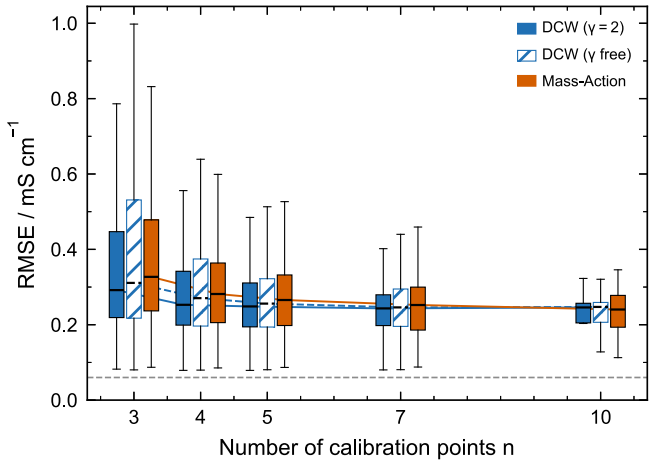

Figure 6. Prediction RMSE vs. number of calibration concentrations n. Box plots show the distribution across all sampled n-point combinations and 11 temperatures for DCW with $\gamma = 2$ (solid blue), DCW with γ free (hatched blue), and mass-action (solid orange). Grey dashed line: median experimental reproducibility (0.06 mS cm^{-1}).

The box-plot whiskers reveal a large spread at small n. This spread arises when calibration concentrations cluster in a narrow range (e.g., below 1.0 mol L^{-1}), forcing the auxiliary $\eta(c)$ and $\rho(c)$ polynomials to extrapolate.[24] The specific three-point protocol (0.25, 1.20, and 3.00 mol L^{-1}) avoids this by anchoring calibration at the domain boundaries. All intermediate predictions remain strictly interpolative, yielding an RMSE of 0.27 mS cm^{-1}—below the $n = 3$ median for all three model variants.

Measurement quality control and automated analysis.—The DCW equation can also serve as an internal consistency check for conductivity measurements. For any combination of c, η, and ρ, the model predicts the expected σ. Measured values deviating by more than the characteristic RMSE (0.24 mS cm^{-1} for the full model, 0.27 mS cm^{-1} for three-point calibration) are flagged as potential outliers. In practice, η and ρ are measured first, the expected σ is calculated *a priori*, and the result is compared with the subsequent EIS measurement. A systematic deviation across multiple temperatures at one concentration indicates a sample preparation error (e.g., incorrect salt mass or moisture ingress). A single-point deviation more likely reflects an isolated measurement artifact. This diagnostic is particularly valuable for high-throughput electrolyte screening,[21] where many individual measurements increase the risk of undetected errors.

Practical protocol for conductivity parameterization.—The analysis above suggests a two-stage protocol that balances laboratory effort against model robustness.

*Stage 1—Screening (*n = *3,* γ = *2 fixed).*—For rapid characterization of a new electrolyte:

1. Prepare electrolyte samples at three concentrations spanning the domain of interest (recommended: 0.25, 1.20, and 3.00 mol L^{-1}).
2. Measure σ, η, and ρ at each concentration across the desired temperature range.
3. Interpolate $\eta(c)$ and $\rho(c)$ via second-order polynomials in c at each temperature.
4. Calibrate the DCW model with $\gamma = 2$ fixed: fit A and α by linear regression of $\log_{10}\sigma - 2\log_{10}\rho$ vs. $\log_{10}(c/\eta)$.
5. Predict σ at any intermediate concentration using the interpolated $\eta(c, T)$ and $\rho(c, T)$ polynomials.

The expected RMSE is ≈0.27 mS cm^{-1} (see above). This stage requires only three electrolyte samples and standard laboratory equipment: an EIS setup and a Stabinger-type viscometer with integrated density cell.[36] Fixing $\gamma = 2$ is recommended at this stage because the sparse density variation at $n = 3$ biases the free-γ estimate (see the resampling analysis above).

*Stage 2—Validation (*n = *5,* γ *free).*—When the electrolyte has a different solvent composition from the training system, the assumption $\gamma = 2$ may not hold (cf. the literature validation above). Two additional concentrations (e.g., 0.50 and 2.00 mol L^{-1}) provide sufficient density variation to constrain γ as a free parameter. At $n = 5$, the median RMSE difference between $\gamma = 2$ and γ free is only 3 % (see the resampling analysis above).

The validation step serves two purposes. First, if the unconstrained γ is consistent with 2 within its standard error, the Stage 1 result is confirmed. Second, if γ deviates significantly from 2, the system-specific value improves the accuracy for that particular solvent system. Beyond five concentrations, additional measurements yield negligible improvements relative to experimental noise (see the resampling analysis above).

Optionally, the model prediction can be used as a real-time consistency check for subsequent conductivity measurements. Deviations exceeding the characteristic RMSE indicate potential sample preparation or measurement errors (see the quality-control procedure above).

Conclusions

We derived a density-corrected Walden (DCW) equation that extends the classical Walden rule by a ρ^2 correction term, halving the RMSE from 0.039 to 0.020 log-units. The model contains two free parameters and is calibratable by linear regression. A complementary mass-action model, adapted from the classical ion-association equilibrium[18,19], separates ion pairing (K_a) from ionic mobility (α_W) at comparable accuracy.

Using only three calibration concentrations, the DCW model reconstructs the full $\sigma(c, T)$ surface with an RMSE of 0.27 mS cm^{-1}. In extrapolation beyond the training range, it is two to three times more accurate than the Casteel–Amis and Landesfeind benchmark equations.

Cross-validation on LiFSI in three pure solvents confirms transferability for $\varepsilon_r > 20$, covering typical multi-component battery electrolytes. The $\gamma = 2$ constraint is system-specific and should be verified for each new solvent composition. We recommend a two-stage protocol: Stage 1 ($n = 3$, $\gamma = 2$ fixed) for rapid screening, Stage 2 ($n = 5$, γ free) for validation. The deterministic σ–η–ρ link additionally enables real-time quality control of conductivity measurements.[21] Extending this framework to the apparent diffusion coefficient and transference number could further accelerate the full transport characterization of emerging electrolyte chemistries.[10,40]

Acknowledgments

M.G. gratefully acknowledges Mercedes-Benz AG, Corporate Research, for supporting this work as part of his doctoral studies.

ORCID

Maximilian Gruber https://orcid.org/0009-0004-3621-2782
Daniel Rutz https://orcid.org/0000-0001-9612-0717
Frank Hofmann https://orcid.org/0009-0005-4315-7213
André Weber https://orcid.org/0000-0003-1744-3732

References

1. K. Xu, *Chem. Rev.*, **104**, 4303 (2004).
2. K. Xu, *Chem. Rev.*, **114**, 11503 (2014).
3. J. Newman and K. E. Thomas-Alyea, *Electrochemical Systems* (John Wiley & Sons, Hoboken, NJ) 3rd ed. (2004).
4. B. Boz, T. Dev, A. Salvadori, and J. L. Schaefer, *J. Electrochem. Soc.*, **168**, 090501 (2021).
5. L. O. Valøen and J. N. Reimers, *J. Electrochem. Soc.*, **152**, A882 (2005).
6. A. Nyman, M. Behm, and G. Lindbergh, *Electrochim. Acta*, **53**, 6356 (2008).
7. M. Doyle, T. F. Fuller, and J. Newman, *J. Electrochem. Soc.*, **140**, 1526 (1993).

8. T. F. Fuller, M. Doyle, and J. Newman, *J. Electrochem. Soc.*, **141**, 1 (1994).
9. J. Landesfeind and H. A. Gasteiger, *J. Electrochem. Soc.*, **166**, A3079 (2019).
10. D. T. Hickson, D. M. Halat, A. S. Ho, J. A. Reimer, and N. P. Balsara, *Phys. Chem. Chem. Phys.*, **24**, 23433 (2022).
11. J. F. Casteel and E. S. Amis, *J. Chem. Eng. Data*, **17**, 55 (1972).
12. A. de Diego, J. M. Madariaga, and E. Chapela, *Electrochim. Acta*, **42**, 1449 (1997).
13. M. S. Ding, K. Xu, and T. R. Jow, *J. Electrochem. Soc.*, **152**, A132 (2005).
14. K. L. Gering, *Electrochim. Acta*, **225**, 175 (2017).
15. A. Dave, K. L. Gering, J. M. Mitchell, J. Whitacre, and V. Viswanathan, *J. Electrochem. Soc.*, **167**, 013514 (2020).
16. Y. Liu, B. Guo, X. Zou, Y. Li, and S. Shi, *Energy Storage Mater*, **31**, 434 (2020).
17. A. K. Mishra, S. Rajput, M. Karamta, and I. Mukhopadhyay, *ACS Omega*, **8**, 16419 (2023).
18. R. A. Robinson and R. H. Stokes, *Electrolyte Solutions* 2nd ed ed.(London) (Butterworths) (1959).
19. Y. Marcus and G. Hefter, *Chem. Rev.*, **106**, 4585 (2006).
20. J. Neuhaus, E. von Harbou, and H. Hasse, *J. Power Sources*, **394**, 148 (2018).
21. F. Rahmanian, M. Vogler, C. Wölke, P. Yan, S. Fuchs, M. Winter, I. Cekic-Laskovic, and H. S. Stein, *Sci. Data*, **10**, 43 (2023).
22. P. Walden, *Z. Elektrochem. Angew. Phys. Chem*, **12**, 77 (1906).
23. J. O. Bockris and A. K. N. Reddy, *Modern Electrochemistry* (Plenum Press, New York) vol 12nd ed. (1998).
24. M. Schammer, B. Horstmann, and A. Latz, *J. Electrochem. Soc.*, **168**, 026511 (2021).
25. W. Xu and C. A. Angell, *Science*, **302**, 422 (2003).
26. C. A. Angell, Y. Ansari, and Z. Zhao, *Faraday Discuss*, **154**, 9 (2012).
27. K. Ueno, H. Tokuda, and M. Watanabe, *Phys. Chem. Chem. Phys.*, **12**, 1649 (2010).
28. A. Apelblat, *J. Phys. Chem. B*, **112**, 7032 (2008).
29. C. L. Berhaut, D. Lemordant, P. Porion, L. Timperman, G. Schmidt, and M. Anouti, *RSC Adv*, **9**, 4599 (2019).
30. S. Han, *Sci. Rep.*, **7**, 46718 (2017).
31. M. Drüschler and B. Huber, (2020), Application note, rhd instruments GmbH & Co. KG, Darmstadt, Germany, available from: https://rhd-instruments.de/en/support/downloads.
32. M. E. Orazem and B. Tribollet, *Electrochemical Impedance Spectroscopy* (John Wiley & Sons, Hoboken, NJ) 2nd ed. (2017).
33. ASTM International, ASTM D7042-21: Standard Test Method for Dynamic Viscosity and Density of Liquids by Stabinger Viscometer (and the Calculation of Kinematic Viscosity), ASTM International, West Conshohocken, PA, (2021), 10.1520/D7042-21.
34. J. Neuhaus, E. Forte, E. von Harbou, and H. Hasse, *J. Power Sources*, **398**, 215 (2018).
35. K. R. Harris, *J. Phys. Chem. B*, **114**, 9572 (2010).
36. for Standardization I O 1996 Crude petroleum and petroleum products—Determination of density—Oscillating U-tube method Tech. Rep. ISO 12185:1996 International Organization for Standardization Geneva, Switzerland.
37. K. Hayamizu, Y. Aihara, S. Arai, and C. G. Martinez, *J. Phys. Chem. B*, **103**, 519 (1999).
38. N. Molinari, J. P. Mailoa, N. Craig, J. Christensen, and B. Kozinsky, *J. Power Sources*, **428**, 27 (2019).
39. T. Uchida and T. Kiyobayashi, *Phys. Chem. Chem. Phys.*, **23**, 10875 (2021).
40. S. Dhir, B. Jagger, A. Maguire, and M. Pasta, *Nat. Commun.*, **14**, 3833 (2023).